THE SEISMOLOGICAL SOCIETY OF AMERICA
400 Evelyn Ave., Suite 201
Albany, CA 94706-1375
(510) 525-5474; FAX (510) 525-7204
www.seismosoc.org

Bulletin of the Seismological Society of America, Vol. 101, No. 5, pp. 2399–2407, October 2011, doi: 10.1785/0120100346

Twenty Thousand Aftershocks of a Very Small (M 2) Earthquake and Their Relation to the Mainshock Rupture and Geological Structures

by Makoto Naoi, Masao Nakatani, Yasuo Yabe, Grzegorz Kwiatek, Toshihiro Igarashi, and Katrin Plenkers*

Abstract We have determined the locations of more than 20,000 aftershocks (as small as moment magnitude M_w −4.4 or even smaller) following an M 2 event in a South African gold mine, using manually picked arrival times. Spatial clustering into five groups was clearly discerned. A majority of the aftershocks formed a planar cluster (~4 m in apparent thickness, ~100 × 80 m in areal extent). This cluster is thought to delineate the rupture area of the mainshock because its orientation and spatial extent were consistent with the nodal plane of the centroid moment tensor (CMT) solution and with the corner frequency of the mainshock, respectively. The cluster's attitude suggests that the mainshock was a Mohr–Coulomb failure (or formation of a shear rupture surface in intact rock at an angle that obeys the Coulomb failure criterion) that took place in a vertical compression stress field that is indicated by borehole breakout patterns. The aftershock distribution also shows that the mainshock rupture was largely confined to the interior of a 25-m-thick vertical dike, although there are indications of interactions taking place between the rupture and the dike's material boundary with the host rock.

Introduction

Thousands of aftershocks delineating the mainshock rupture plane are a common observation for $M \geq 7$ earthquakes. Aftershock distributions therefore provide useful information on fault/rupture configurations, geological structures, and interactions between them (e.g., Kato *et al.*, 2007). For small and midsized ($M \leq 5$) earthquakes, distinctly planar aftershock distributions have rarely been observed. The reported aftershock distributions are often scattered over finite volumes, but this can be an artifact of the insufficient location accuracy and sensitivity of the seismic networks. Some studies suggest, however, that the characteristics of aftershock occurrence may depend on the mainshock magnitude (e.g., Ouillon and Sornette, 2005). Aftershocks delineating a rupture plane are thought to be generated by stress disturbance due to the irregularity of the mainshock rupture (Helmstetter and Shaw, 2006; Marsan, 2006). Knowledge of the potential mainshock size dependency of aftershock activities is therefore expected to provide information on the scaling relationship of the complexity of mainshock rupture (Bouchon and Karabulut, 2008).

To study the aftershock activities of small and midsized earthquakes on the same level of resolution relative to the mainshock rupture size as in the case of large ($M \geq 7$) earthquakes, the aftershocks need to be observed down to magnitudes smaller by 5 to 6 than that of the mainshock, and their location accuracy needs to be smaller than several percent of the mainshock rupture size. Deep gold mines in South Africa, where up to M 3 mining-induced earthquakes frequently occur, offer a realistic possibility to meet this requirement. In mines, it is possible to deploy dense seismic arrays in the prospective source region of M 2 to M 3 earthquakes, because earthquake timing and location can be anticipated on the basis of stress buildup calculated from mining plans. It is established that these mining-induced earthquakes (except for earthquakes in heavily damaged rocks near human-made cavities) are shear ruptures similar to natural earthquakes (e.g., Spottiswoode and McGarr, 1975; McGarr *et al.*, 1981; Yamada *et al.*, 2005a,b; Yamada *et al.* 2007).

Previous studies of earthquakes in mines mainly targeted magnitudes between −1 and 3, and the seismic networks used could detect only a small number (at most tens) of aftershocks for a mainshock on the order of $M \sim 2$ (e.g., Ogasawara *et al.*, 2002). To better detect smaller earthquakes, the joint Japanese–German Underground Acoustic Emission Research in South Africa (JAGUARS) group has deployed a highly sensitive and dense network (Fig. 1; Nakatani *et al.*, 2008; Plenkers *et al.*, 2010), mainly consisting of piezoelectric-type

*Now at Swiss Seismological Survey, ETH Zurich, Sonneggstrasse 5, 8092 Zürich, Switzerland.

acoustic emission (AE) sensors. This network could detect ruptures at least as small as moment magnitude M_w −4.4 (Kwiatek *et al.*, 2010). An M 2 earthquake took place at a distance of only 30 m above the center of our AE network, and more than 20,000 aftershocks were recorded within 150 hr of its occurrence (Yabe *et al.*, 2009).

Yabe *et al.* (2009) demonstrated that part of these aftershocks had planar alignment similar to the case of aftershocks that accompany $M > 7$ earthquakes and pointed out that this likely delineated the mainshock rupture plane. However, their hypocenter determination was based on automatically picked arrival times that contained a multitude of mispicks, and so their AE catalog remained wanting in both accuracy and reliability, which precluded Yabe *et al.* (2009) from making more in-depth discussions of the aftershock distribution. In the present paper, we relocate the hypocenters using manual picks and use a reliable hypocenter distribution to describe detailed structures of the aftershock distribution. The 2D aftershock distribution, discernible in the relocated hypocenters, demonstrated good agreement with seismic source parameters obtained from waveform analysis of the mainshock. The stress field in the source region, as indicated by borehole breakout and strainmeter data, and the attitude of the estimated rupture surface indicated that the rupture plane of this M 2 event had been formed in intact rock at an angle that obeyed the Coulomb failure criterion. This conclusion is also supported by the discovery of an aftershock alignment that appears to indicate a conjugate fault to the estimated M 2 rupture plane. The aftershock distribution also delineated detailed fault geometry of the M 2 event, including a bend and branching, and indicated the presence of interactions between the mainshock rupture and structural boundaries.

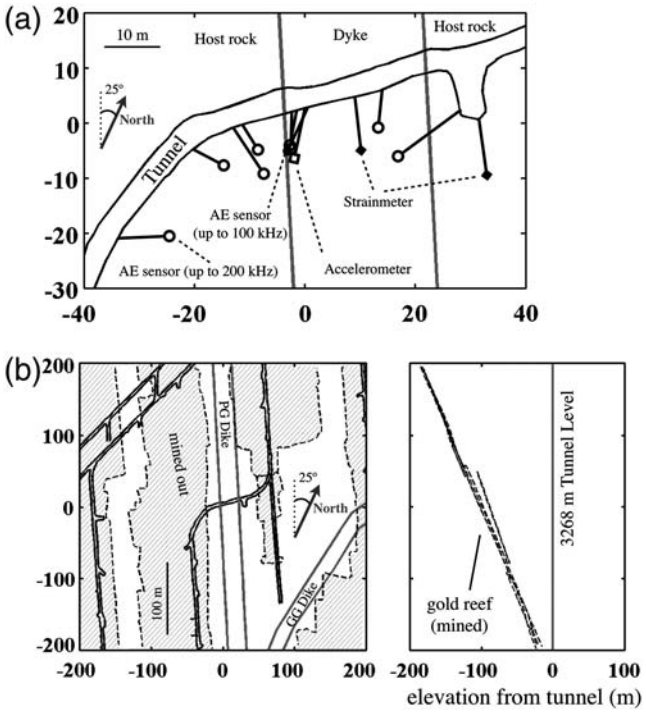

Figure 1. Observation network deployed at the Mponeng gold mine, South Africa, to detect very small fractures. (a) Station layout of the AE network. Black solid lines, boreholes used to install the sensors. Circles, AE sensors (open circles: up to 200 kHz; filled circle: up to 100 kHz). Open square, accelerometer. Filled diamonds, strainmeters. (b) Geology and mining stope geometry in the neighborhood of the network. Areas bounded by broken contours and filled with diagonal lines, cavities mined-out by December 2007. The coordinate system is so defined that the y-axis is parallel to the direction of dip of the gold reef that slopes at about 26.5° to the south-southeast. The broken lines in the side view on the right correspond to the broken lines in the plan view on the left. The origin of the depth coordinate is taken at the depth of the tunnel in which the network is deployed (3268 m deep).

Overview of the Aftershock Distribution

AE Aftershocks and Data Processing

Our AE network consists of eight borehole AE sensors and one three-component accelerometer (Fig. 1a). Seven of the AE sensors cover frequency ranges up to 200 kHz, whereas the other one covers only up to 100 kHz. The accelerometer has flat frequency characteristics from 2 Hz to 25 kHz. The waveforms are recorded by a 16-channel AE monitoring system developed by Gesellschaft für Materialprüfung und Geophysik (GMuG mbH; see, e.g., Manthei, 2005). After being band-pass filtered (1–180 kHz for the AE sensors and 0.05–25 kHz for the accelerometer), the waveforms of all channels are recorded at a sampling rate of 500 kHz over a duration of ~65 ms (32,768 samples). This recording system has a dead time of ~0.3 s following a trigger.

The M 2 mainshock occurred on 27 December 2007. Because the date fell during the Christmas holidays, the records of aftershocks were not contaminated by noise related to mining works. Unfortunately, waveforms of the aftershocks that took place within the first 4.5 hr of the mainshock were lost due to overloading of the hard disk. However, waveforms were obtained for 25,079 triggers that took place within 150 hr of the mainshock. We picked P- and S-wave arrival times manually from each record.

The arrival times were determined by the following procedure. P and S arrivals were picked manually with ~0.1 ms accuracy and associated to the same event by comparison with theoretical arrival times. When more than one event was recorded within a single waveform, we picked arrival times for only one of the events (usually, the event with the largest amplitude). We then applied the algorithm of Takanami and Kitagawa (1988) to the waveform in the neighborhood of each pick. In this method, a seismogram for which an arrival time has to be determined is divided into two parts, and different autoregressive models are applied to the former part and the latter part. The point of division that minimizes the sum of the Akaike information criteria (Akaike, 1973) of the former part and the latter part is identified as the arrival time of a seismic phase. This operation has enabled us to determine arrival times at an eventual accuracy of about 0.04 ms.

We used the Levenberg–Marquardt nonlinear least squares algorithm (Levenberg, 1944; Marquardt, 1963) for aftershock location. Residuals were calculated, with *S* arrivals given only half the weight of *P* arrivals. Our AE network spreads across both sides of a nearly vertical plane of contact between the host rock and a 25-m-thick, platelike gabbroic dike, a major geological structure that is known to continue for more than a kilometer. The elastic wave velocities in the dike and in the host rock were estimated by *in situ* transmission tests (Naoi *et al.*, 2008; Yabe *et al.*, 2009). In aftershock locations, we assumed seismic velocities of 6.45 km/s for *P* waves and 3.79 km/s for *S* waves, each being the average of the value in the dike and the value in the host rock. To avoid local minima, we repeated the location procedure with 125 different initial hypocenters and chose the optimal result for each event.

We analyzed 21,112 aftershocks that satisfied the following conditions: (1) the hypocenters are located within a $400 \times 400 \times 300$ m cuboid volume that is shown in Figure 2; (2) at least four *P* arrivals were picked; (3) at least four *S* arrivals were picked; (4) the root mean square (rms) residual of arrival times is less than 0.2 ms. The average location uncertainty was about 5 m for events that took place 200 m away from the center of the AE network and about 1 m for events that took place within 40 m. The mine's routine seismic observation network, which can detect earthquakes as small as $M_w - 1.5$, recorded only 28 aftershocks in the same area and during the same period, less than 0.2% of the number of aftershocks detected by our AE network.

To evaluate the influence of ignoring the difference in elastic velocities between the dike and the host rock, we relocated all 21,112 hypocenters by a grid search procedure using a medium model with a velocity contrast. Location results differed to some extent (by ~3 m for events that took place within 40 m of the center of our AE network and ~15 m for events 100 m away). Notably, locations using the nonuniform medium model produced spurious alignment of hypocenters along the velocity boundary. This sort of artifact often turns up when hypocenters on the higher-velocity side are located using stations on the lower-velocity side. To avoid this artifact, we use, in the present study, the hypocenter locations determined under the uniform medium model. All characteristics of the aftershock distribution, described in the following paragraphs, were also recognized in the results of locations using the nonuniform medium model.

The use of manually picked arrival times has significantly enhanced the accuracy and reliability of the AE catalog. Yabe *et al.* (2009), who relied on automatically picked arrival times, used criteria stricter than this paper's for hypocenter selection (at least 4 *P*-arrival picks; at least 4 *S*-arrival picks; at least 10 *P*- and *S*-arrival picks combined; at most 0.2 ms in rms residuals) in order to eliminate hypocenters that were located away from their true locations due to mispicks. Out of the AE events for which they determined the hypocenters using automatic picks, 10,239 occurred within the same study period as in the present study (between 4.5 hr and 150 hr after the mainshock), were located within the same domain, and satisfied the stricter criteria stated previously. (These include events that are not discussed in the Yabe *et al.*, 2009 paper, because the study domain is broader.) By contrast, 20,771 of the hypocenters relocated in the present study satisfied the stricter criteria. Figure 3 shows histograms of rms residuals for these two data sets. It demonstrates that enhanced accuracy in arrival time picks has shifted the most frequent residuals toward smaller values. The reader may also note that, for the discussion of aftershock clustering to follow in the present paper, it is essential not only to use aftershocks that were located with high precision, but also to use as exhaustive a set as possible of all earthquakes that actually occurred. The catalog used by Yabe

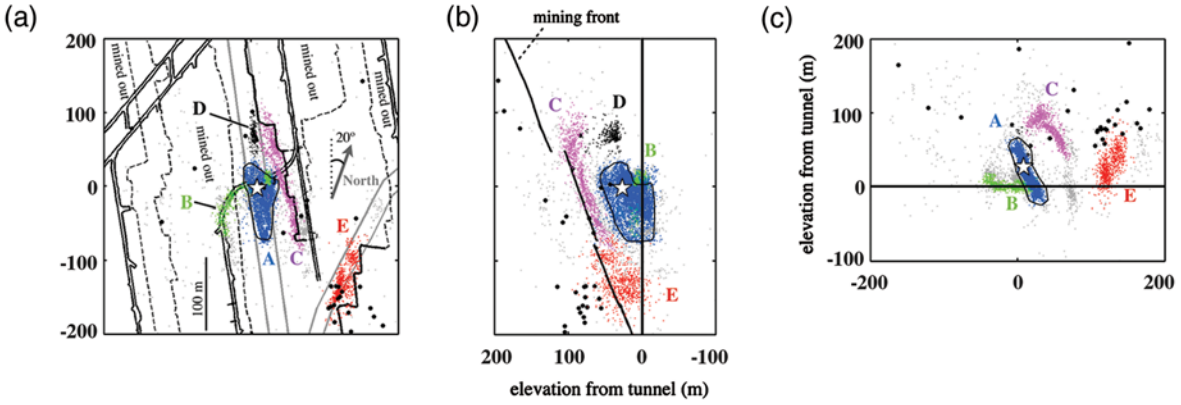

Figure 2. Distribution of aftershocks of the *M* 2 earthquake on 27 December 2007. Small dots show aftershocks located by our AE network (different colors for different clusters). (a) Plan view. (b, c) Side views seen from directions that are normal and parallel, respectively, to the strike of the main aftershock cluster (blue dots encircled by a black solid contour). At first glance of (a), it may appear that the *y*-axis is not aligned to the strike of the main cluster, but this is so because the height of the upper end of the cluster varies with the *y* location. Large black dots show aftershocks detected by the mine's routine observation network. The star is the rupture initiation point of the *M* 2 event. Thick gray lines show planes of contact between dikes and the host rock. Narrow paths drawn in black are the access tunnels running at a depth of 3268 m. Broken contours in (a) show mining fronts of the mined-out cavities shown in Figure 1. Lateral projection of the part emphasized in bold black lines in (a) is shown in (b).

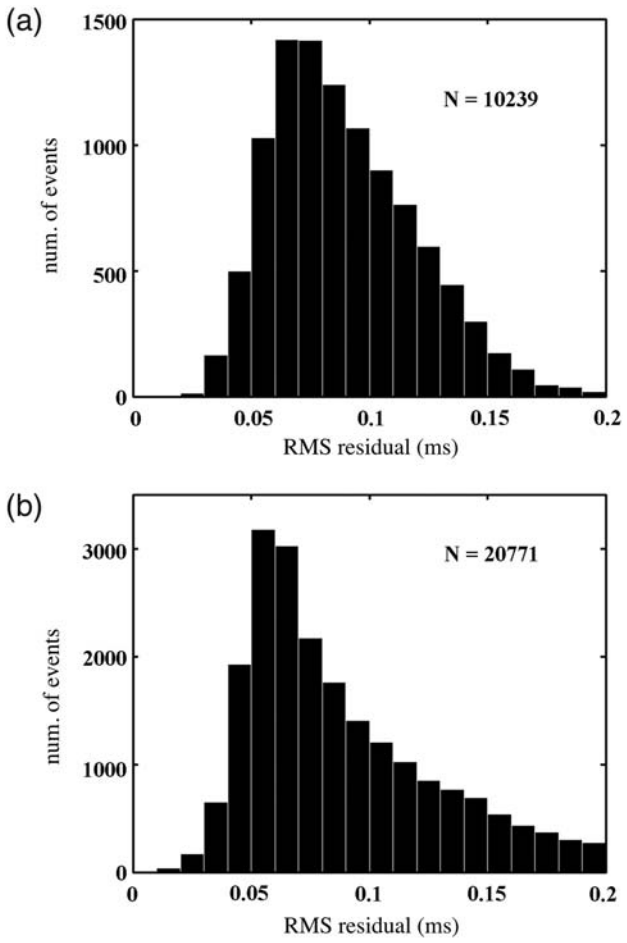

Figure 3. Histograms of rms residuals for the aftershocks that occurred between 4.5 hr and 150 hr after the *M* 2 mainshock. The plots are shown for events which satisfy the criteria of at least four *P*-arrival picks, at least four *S*-arrival picks, at least 10 arrival picks in total and at most 0.2 ms in rms residual, and whose hypocenters were located within the domain shown in Figure 2. (a) Results for automatically picked arrival times. (b) Results for manually picked arrival times.

et al. (2009) missed more than 10,000 events that could have been detected by using manual picks.

Aftershock Clusters

The aftershocks detected by our AE network clearly demonstrate spatial clustering into five groups (A–E in Fig. 2). Few aftershocks occurred outside of these five clusters. Clusters A–E were made up of 12,562; 4549; 1146; 357; and 813 events, respectively. Temporal decay of the aftershock occurrence rate followed the modified Omori's law for each of the five clusters (Fig. 4), indicating that those clusters were aftershocks of the *M* 2 event. The Omori exponent *p* is apparently close to 1 for all clusters.

Cluster A (hereafter referred to as the main cluster) included 60% of the aftershocks and showed a planar distribution dipping 60° to the east. As mentioned by Yabe *et al.* (2009), this seems to delineate the mainshock rupture area. A subhorizontal borehole, drilled 1.5 years after the mainshock, showed near-horizontal breakout of the wall in the neighborhood of the fault, which implies a vertical compression stress field. On the basis of these observations, Yabe *et al.* (2009) pointed out that the *M* 2 rupture was apparently a Mohr–Coulomb failure; in other words, the vertical compressional stress created a shear fracture plane in intact rock at a dip angle of ~60° in compliance with the Coulomb failure criterion (corresponding to an internal friction coefficient of 0.6). Cluster A is located in a solid rock mass at a distance from mined-out cavities and tunnels, so it appears reasonable to consider that this *M* 2 event was driven by an overall stress field spanning the scale of the entire mainshock rupture area, not by local stress concentration in the immediate vicinity of a cavity. As shown in the next section, we give further support for this interpretation. Two sets of Ishii's three-component strainmeters (Ishii *et al.*, 1997) were installed in subhorizontal boreholes to monitor stress changes (Fig. 1a; one in the dike, another in the host rock to the east). Both strainmeters indicated near-vertical compression (Katsura, 2009), in agreement with the orientation of the mainshock failure. Strain changes, recorded over seven months before the mainshock, showed a subvertical stress increment of 11.9 MPa in the dike and 7.8 MPa in the host rock (Katsura, 2009; Hirano, 2010, personal commun.).

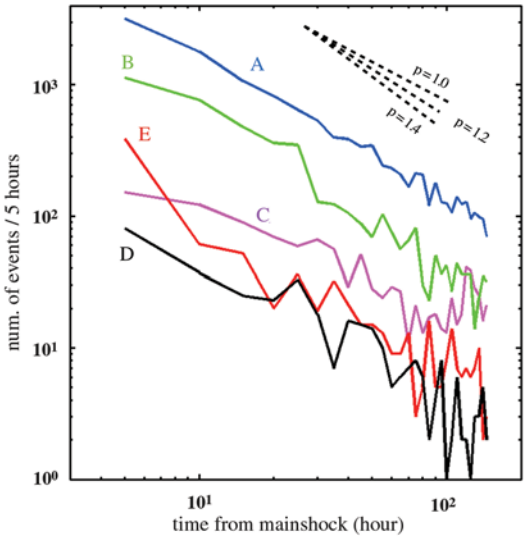

Figure 4. Temporal decay of the aftershocks in each cluster. Different colors are used for clusters A–E. Dashed lines show slopes corresponding to different Omori exponents.

Clusters B, C, and E are located near borders of man-made cavities. The aftershocks are concentrated distinctly along an access tunnel for cluster B and in front of mined-out cavities about 1 m thick for clusters C and E. In Figure 2b, the AE alignment of cluster C appears to be located below a mined-out cavity, but it seems likely that this is an artifact of systematic biases due to the presence of unmodeled velocity structures; the aftershocks were actually occurring on the same height level. In fact, we have confirmed that the alignment of cluster C was determined at approximately the same depths as the mining front, shown in Figure 2b,

if the hypocenters were relocated by assigning different seismic wave velocities to the dike and to the host rock, respectively. In the map view (Fig. 2a), the aftershocks in cluster E appear to be distributed largely along the mining front, but in the side views (Fig. 2b,c), they are scattered over broader regions. We might hypothesize that this is because of the large hypocenter location errors in the vertical direction near cluster E that are due to both the large separation of this cluster from the observation network and the east–west alignment of the station layout, and that the aftershocks were actually concentrated in the neighborhood of the cavity.

The enhanced aftershock activities in the proximity of cavities are presumably due to enhanced sensitivity to stress changes caused by local stress concentration near cavities and also by damages in rocks in front of the mining developments. (In mines, cavities are developed by dynamite blowup, which heavily damages rocks in their surroundings.) In fact, AE occurrences used to be more active in regions B, C, and E than elsewhere during normal times prior to the M 2 event. There is no man-made cavity near aftershock cluster D, and it remains uncertain why it is there, but this region was also home to high AE activity during normal times.

Analysis of the Mainshock Rupture

Centroid Moment Tensor Inversion

The routine seismic network of the Mponeng mine consists largely of 4.5 Hz three-component borehole geophones, installed at intervals of about 500 m on average. We calculated the centroid moment tensor (CMT) solution of the M 2 mainshock using waveform records from this network. The three channels of these geophones are supposed to be oriented north–south, east–west, and up–down, respectively; but as sometimes happens, during repeated maintenance works their polarities get reversed or different channels get crossed. In CMT analysis, we used waveform records from nine geophones whose polarities and channel settings could be checked and corrected if necessary, by comparing waveforms of distant earthquakes recorded at neighboring stations. Consistency between P-wave first motions and ray directions was also checked. Figure 5 illustrates locations of the nine geophones used for the inversion. We calculated the six independent components of the moment tensor under a homogeneous medium model and with a triangular source time function. Fitting was performed on ~0.2 s long portions of waveforms that included P-arrival times, band-pass filtered between 4 and 10 Hz. The variance reduction was 61%. S waves were not used because of wave-splitting problems, but the first motion polarities and amplitudes of the synthetic S waves were generally consistent with the observations. One of the CMT nodal planes (Fig. 5) strikes N5.9° W and dips 56°, which is very similar to the orientation of the main aftershock cluster. The rake was −57°, which indicates normal faulting. The moment magnitude was estimated at 2.2 ($M_0 = 2.9 \times 10^{12}$ N m).

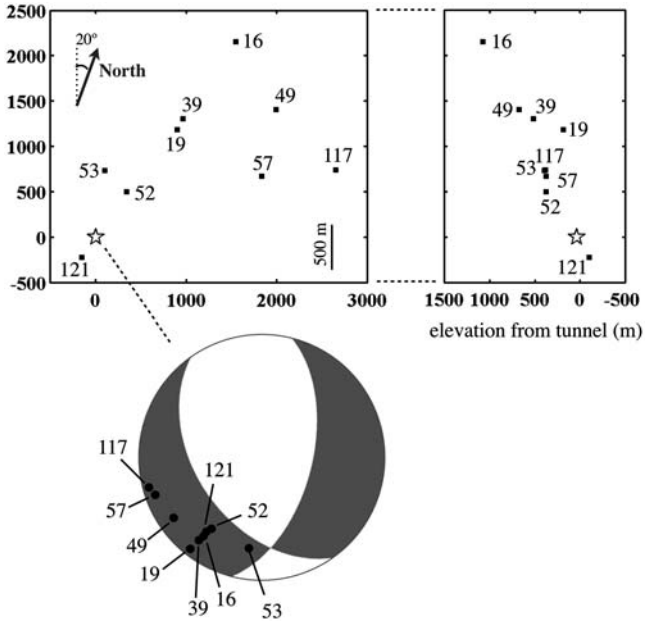

Figure 5. Station layout used for the CMT analysis of the M 2 mainshock and the CMT solution. Top left, plan view. Top right, side view. The coordinate axis is defined as in Figure 2. Star, mainshock hypocenter. Filled squares, stations of the mine's routine seismic network used for the inversion. Numbers beside the stations, station IDs. Bottom, focal mechanism of the M 2 event shown in lower hemisphere projection (nondouble couple components were negligible). The dots within the push domain, painted gray, represent the station locations projected onto the focal sphere.

Estimating the Rupture Initiation Point of the M 2 Earthquake

The location of the M 2 mainshock as determined by the mine's network was not very accurate (uncertainty ~20 m). The uncertainty was especially large in the vertical direction because the mine's network has a subhorizontal station layout that follows the planar geometry of the gold reef. Although our AE network had much better location accuracy near the M 2 hypocenter, it could not locate the mainshock very well, because the S-wave arrival times could not be picked due to waveform saturation. So we attempted to estimate the rupture initiation point of the mainshock by searching for aftershocks that have a pattern of P-wave arrival times similar to that of the mainshock.

We define the arrival time residual t_{res} as follows:

$$t_{\mathrm{res}} = \sqrt{\sum_{i}^{n} (T_i^{\mathrm{after}} - T_i^{\mathrm{main}} - \Delta T)^2},$$

$$\Delta T = \frac{1}{n} \sum_{i}^{n} (T_i^{\mathrm{after}} - T_i^{\mathrm{main}}).$$

T_i^{after} is the P-wave arrival time of an aftershock at the ith station, T_i^{main} is the P-wave arrival time of the M 2 mainshock, and n is the number of stations. We calculated t_{res} for 5924 well-located aftershocks that satisfied the following conditions: (1) the hypocenters are located within 80 m of the

center of our AE network; (2) at least seven *P* arrivals were picked; (3) at least seven *S* arrivals were picked; (4) the rms residual of arrival times is less than 0.1 ms. Twenty-eight of the events had t_{res} smaller than 0.04 ms. These events were concentrated within a radius of 5 m of a location 30 m above the center of our AE network. We regard the mean coordinates of those events as the rupture initiation point of the *M* 2 mainshock (star in Fig. 2). The horizontal location of this point is very close to that of the mainshock as determined by the mine's routine network.

Corner Frequency of the Mainshock and the Spatial Extent of the Main Aftershock Cluster

Using *S*-wave seismograms of the mine's network, we obtained a corner frequency of 15 Hz for the mainshock. This converts to a rupture radius of $r = 75$ m, if we assume the circular crack model of Sato and Hirasawa (1973) and a rupture velocity of 90% of the *S*-wave velocity. This length is consistent with the spatial extent of the main aftershock cluster (~100 × 80 m). This result, together with the CMT solution and the rupture initiation point described previously, leads us to believe that the main aftershock cluster delineated the rupture area of the *M* 2 mainshock.

According to the formula of Eshelby (1957), the previously mentioned values of M_0 and *r* correspond to a stress drop of 3 MPa. This falls in typical ranges for natural earthquakes (e.g., Kanamori and Anderson, 1975) and mining-induced earthquakes (e.g., Yamada *et al.*, 2007).

Details of the Main Aftershock Cluster

Figure 6 shows vertical cross sections of the main aftershock cluster sliced at 10-m intervals. Contact surfaces on both sides of the platelike dike were each modeled as a single plane that passes approximately through dike contacts that had been discovered in boreholes at 12 locations within 150 m of our AE network. Their dip and strike angles, thus

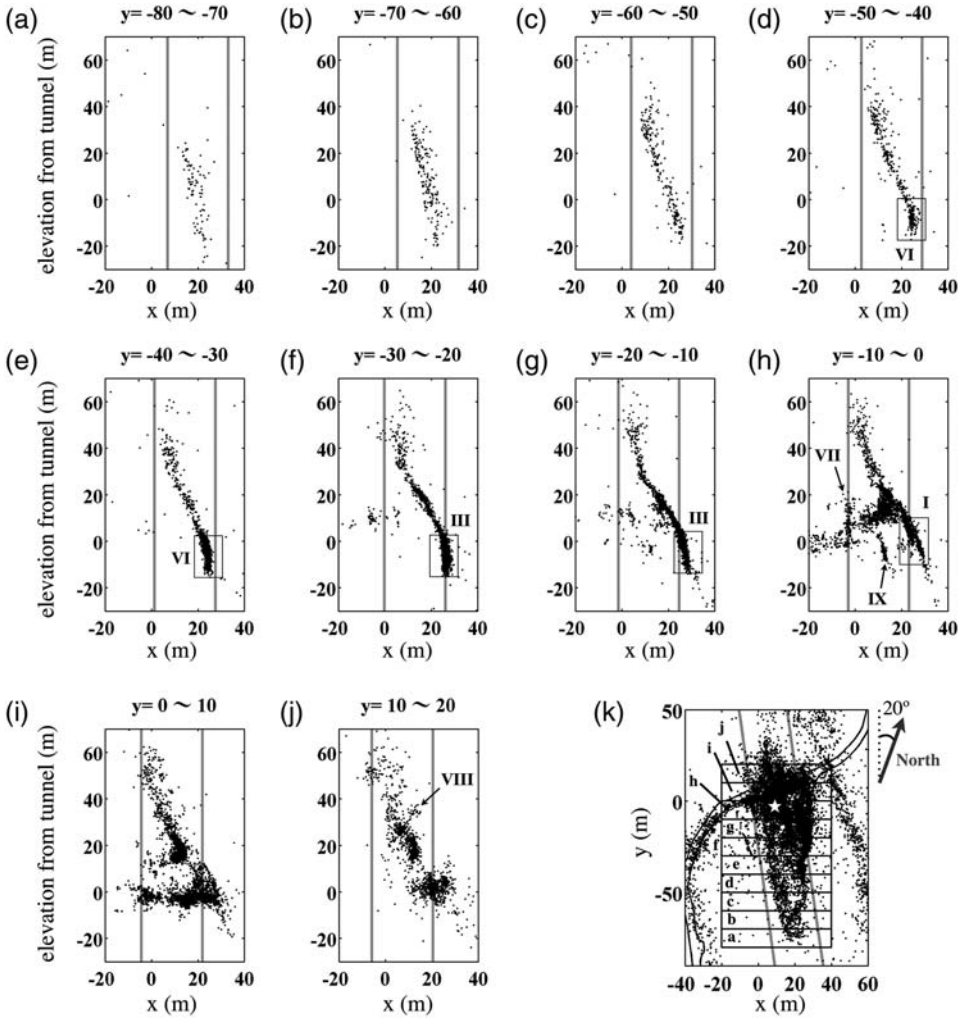

Figure 6. (a–j) Vertical cross sections of areas near the main aftershock cluster sliced at 10-m intervals. (k) Plan view of the main aftershock cluster (zoom of the map view in Fig. 2), with boxes showing the locations of slices in panels (a–j) . The gray lines show planes of contact between the dike and the host rock. The stars in (h) and (k) show the rupture initiation point of the mainshock.

determined, are consistent with those of the dike, which is known to continue over more than 1 km.

An aftershock alignment, which is thought to delineate the mainshock rupture area, stands out in all cross sections as a thin zone crossing the dike at an angle of about 60°. The rupture of the *M* 2 earthquake seems to have been largely confined to the interior of the dike despite the presence of geological boundaries nearby. In addition, the rupture initiation point also lies within the dike. Figure 7 shows cross sections sliced at 2-m intervals. The planar aftershock zone has an apparent thickness of about 4 m, only several percent of its length (~100 m). Areas adjacent to this narrow zone were mostly quiet.

Within the main aftershock cluster, location uncertainties are so small that even more details can be recognized. In area I in Figures 6 and 7, two branches are visible. The major branch continues out from the 60°-dipping alignment within the dike, whereas the minor branch tends vertically down along the east contact of the dike. This branch can also be recognized in plan view maps that show that the minor branch runs closely along the dike contact (II in Fig. 8c,d). This probably represents subsidiary faulting on the contact plane that took place during the mainshock rupture.

South of where this branching takes place (Fig. 6f,g), the main aftershock cluster bends downward near the location where it crosses the east contact of the dike; at depths of −15 m to 5 m, it runs almost parallel to, or on top of, the contact plane (III in Fig. 6f,g). Plan view maps show (IV in Fig. 8c, d) that this continues straight out from the minor branch in area II (i.e., striking parallel to the dike). The mainshock rupture may have been attracted to the material boundary here. Farther to the south (V in Fig. 8c,d), the aftershock cluster remains within the dike, but the downward bend is still visible (VI in Fig. 6d,e). This possibly indicates that the rupture was attracted to the extensional quadrant of mode II fracture.

There are some smaller-scale (up to 20 m) aftershock alignments that do not seem to belong to the main rupture system. The alignment VII (Fig. 6h), near the west contact of the dike, is limited to the neighborhood of the access tunnel where high stress is expected. Its concentration near the contact may be ascribed to low fracture strengths on the contact plane. The alignment VIII (Fig. 6j) has a planar shape dipping about 60° W, which can be conjugate to the mainshock rupture. This provides another support to the view that the *M* 2 mainshock was a Mohr–Coulomb failure. The alignment X (Fig. 7g) has a 20-m long planar shape dipping ~30° to the southwest. This angle is very different from the optimal angle for Mohr–Coulomb failure, so this alignment may either represent aftershocks of a large aftershock that had a different focal mechanism because of large stress disturbances by the mainshock or represent ruptures on a preexisting weak plane in the dike.

Discussion and Conclusion

The mine's routine network, which could detect aftershocks only as small as $M_w - 1.5$, revealed only one aftershock cluster far to the south of the main rupture (large black dots in Fig. 2). It failed to detect any of the other clusters revealed by our AE network, including the most outstanding one near the mainshock. This implies that larger aftershocks ($M_w > -1.5$) tended to be concentrated in cluster E, whereas most of the aftershocks that occurred elsewhere had smaller magnitudes. The present case illustrates how observation with insufficient sensitivity can lead to a qualitatively different picture of the seismic pattern, rather than a diluted version of well-resolved observation. Kwiatek *et al.* (2010) estimated the M_w of the events detected by our AE network, assuming that the AE sensors function as velocity meters. According to their results, 95% of the aftershocks in the main cluster were

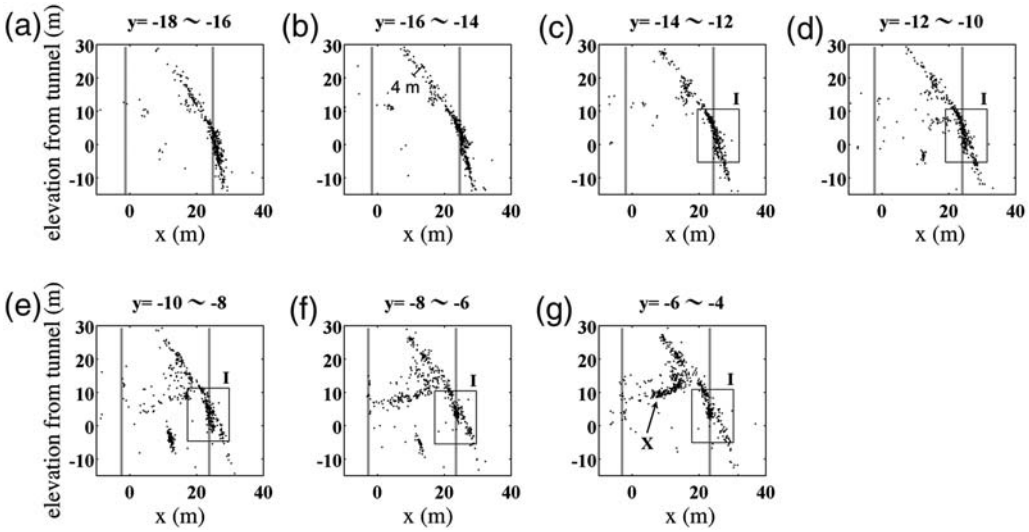

Figure 7. (a) ~g) Vertical cross sections of areas near the main aftershock cluster sliced at 2-m intervals (detailed views of what is shown in Fig. 6).

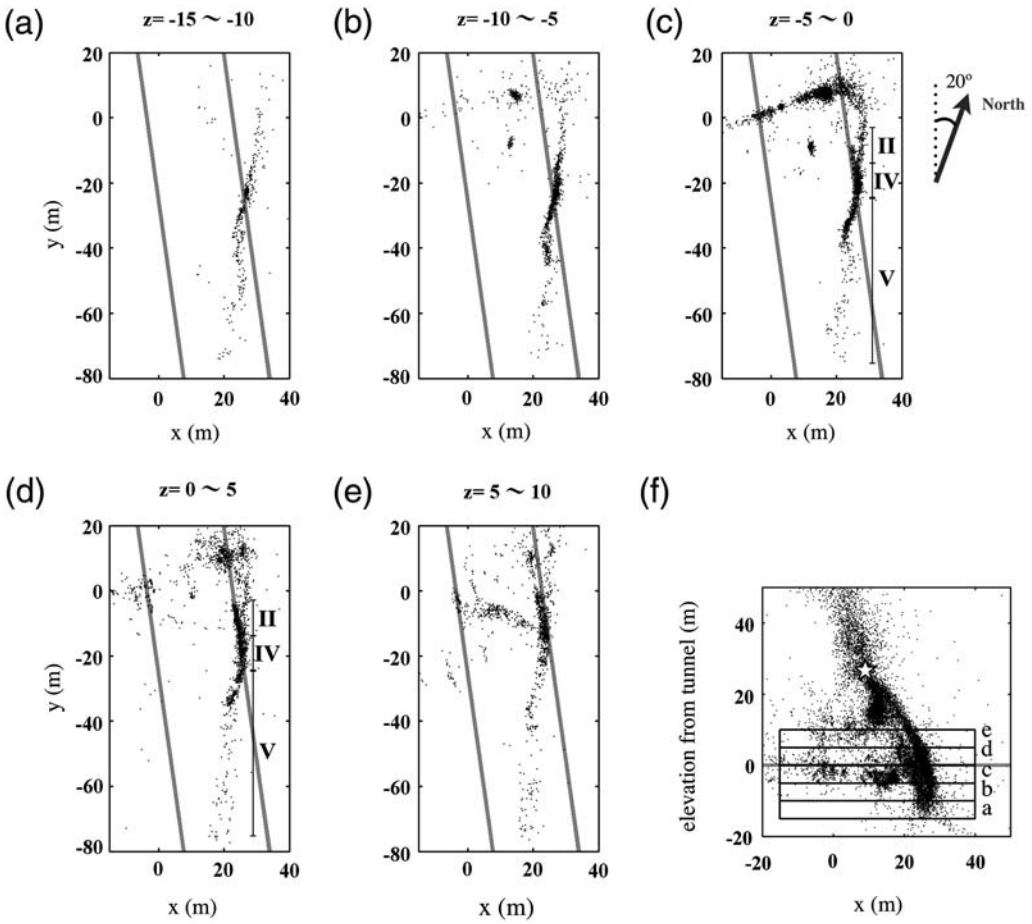

Figure 8. (a–e) Horizontal cross sections of areas near the main aftershock cluster sliced at 5-m intervals. (f) Side view of the main aftershock cluster as seen from the direction of its strike (zoom of the bottom left panel in Fig. 2), with boxes showing the locations of slices in panels (a–e). The star in (f) shows the rupture initiation point of the mainshock.

smaller than $M_w - 3.5$. The lack of aftershock distributions delineating the mainshock rupture area, which has been pointed out for class M 2 earthquakes in earlier studies, may have been a result of insufficient detection capabilities of the networks used.

Yabe *et al.* (2009) suggested, on the basis of the dip angle of the planar aftershock distribution and patterns of borehole breakout, that the M 2 mainshock could have been a Mohr–Coulomb failure that took place in a vertical compression stress field. We have provided further support for this interpretation on the basis of waveform analysis of the M 2 mainshock, distribution of aftershocks located by manually picked arrival times, and the presence of an aftershock alignment that is conjugate to the mainshock rupture plane. The M 2 earthquake's rupture was largely confined to the interior of the dike and dipped at an optimal angle for Mohr–Coulomb failure, despite the presence of clear geological boundaries nearby. Although secondary structures of the aftershock distribution imply that part of the dike's contact planes, where fracture strengths are lower, may also have been broken, the main aftershock cluster indicates the rupture plane orientation was primarily controlled by the stress field.

Data and Resources

Acoustic emission data used in this study were collected by the JAGUARS network in the Mponeng gold mine. JAGUARS is a joint project of the University of Tokyo, Tohoku University, Ritsumeikan University (Japan), GFZ German Research Center for Geosciences, Gesellschaft für Materialprüfung und Geophysik (Germany), Seismogen CC, AngloGoldAshanti Ltd., ISS International, and the Council for Scientific and Industrial Research Johannesburg (South Africa). The seismograms and the earthquake catalog from the mine's monitoring were provided by the Mponeng gold mine. These data are currently not released to the public.

Acknowledgments

We thank S. Ide of the University of Tokyo for use of the CMT inversion program. Technical support by the Mponeng gold mine (AngloGold Ashanti), ISS International Ltd., and the Council for Scientific and Industrial Research Johannesburg is greatly appreciated. Routine seismic data were provided by the Mponeng mine. This work was partly supported by Grants-in-Aid for Scientific Research (A-18253003, A-14204040, B-18403007, A-21246134, 07J09904), a joint research program of the Earthquake Research Institute, a twenty-first century COE Program of

Tohoku University, the Science and Technology Research Partnership for Sustainable Development (SATREPS), and the Observation and Research Program for the Prediction of Earthquakes and Volcanic Eruptions of the Ministry of Education, Culture, Sports, Science and Technology (MEXT) of Japan. Comments by associate editor Arthur McGarr, Geoffrey Ely, and an anonymous referee were instrumental in improving the paper and are cordially appreciated.

References

Akaike, H. (1973). Information theory and an extension of the maximum likelihood principle, in *Proc. of the 2nd International Symposium on Information Theory*, B. N. Petrov and F. Csaki (Editors), Akademiai Kiado, Budapest, 267–281.

Bouchon, M., and H. Karabulut (2008). The aftershock signature of supershear earthquakes, *Science* **320,** no. 5881, 1323–1325, doi 10.1126/science.1155030.

Eshelby, J. D. (1957). The determination of the elastic field of an ellipsoidal inclusion, and related problems, *Proc. Roy. Soc. London, A* **241,** 376–396.

Helmstetter, A., and B. E. Shaw (2006). Relation between stress heterogeneity and aftershock rate in the rate-and-state model, *J. Geophys. Res.* **111,** B07304, doi 10.1029/2005JB004077.

Ishii, H., T. Yamauchi, and F. Kusumoto (1997). Development of high sensitivity bore hole strain meters and application for rock mechanics and earthquake prediction study, in *Rock Stress*, A. A. Balkema, Brookfield, Vermont, 253–258.

Kanamori, H., and D. L. Anderson(1975). Theoretical basis of some empirical relations in seismology, *Bull. Seismol. Soc. Am.* **65,** 1073–1095.

Kato, A., and The Research Team of Aftershock Observations for the 2004 Mid-Niigata Prefecture Earthquake (2007). High-resolution aftershock observations in the source region of the 2004 mid-Niigata prefecture earthquake, *Earth Planets Space* **59,** 923–928.

Katsura, T. (2009). Rock mass deformation before, at and after an *M* 2.1 earthquake within only 20 m from two Ishii strainmeters, *B.S. Thesis*, Ritsumeikan University, Kusatsu, Japan (in Japanese).

Kwiatek, G., K. Plenkers, M. Nakatani, Y. Yabe, G. Dresen, and JAGUARS-Group (2010). Frequency-magnitude characteristics down to magnitude −4.4 for induced seismicity recorded at Mponeng Gold Mine, South Africa, *Bull. Seismol. Soc. Am.* **100,** 1165–1173, doi 10.1785/0120090277.

Levenberg, K. (1944). A method for the solution of certain nonlinear problems in least squares, *Q. Appl. Math.* **2,** 164–168.

Manthei, G. (2005). Characterization of acoustic emission sources in a rock salt specimen under triaxial compression, *Bull. Seismol. Soc. Am.* **95,** 1674–1700, doi 10.1785/0120040076.

Marquardt, D. W. (1963) An algorithm for least-squares estimation of nonlinear parameters, *SIAM J. Appl. Math.* **11,** 431–441.

Marsan, D. (2006). Can coseismic stress variability suppress seismicity shadows? Insights from a rate-and-state friction model, *J. Geophys. Res.* **111,** B06305, doi 10.1029/2005JB004060.

McGarr, A., R. W. E. Green, and S. M. Spottiswoode (1981). Strong ground motion of mine tremors: Some implications for near-source ground motion parameters, *Bull. Seismol. Soc. Am.* **71,** 295–319.

Nakatani, M., Y. Yabe, J. Philipp, G. Morema, S. Stanchits, G. Dresen, and JAGUARS-Group (2008). Acoustic emission measurements in a deep gold mine in South Africa—Project overview and some typical waveforms, *Seismol. Res. Lett.* **79,** no. 2, 311.

Naoi, M., M. Nakatani, Y. Yabe, J. Philipp, and JAGUARS-Group (2008). Very high frequency AE (< 200 kHz) and micro seismicity observation in a deep South African gold mine—Evaluation of the acoustic properties of the site by in-situ transmission test, *Seismol. Res. Lett.* **79,** no. 2, 330.

Ogasawara, H., S. Sato, S. Nishii, H. Kawakata, and The Research Group for Semi-Controlled Earthquake-Generation Experiments in South African Deep Gold Mines (2002). Temporal variation of seismic parameters associated with an $M_w \sim 2$ event monitored at a 100 ∼ 200 m distance, *Seismogenic Process Monitoring* H. Ogasawara, T. Yanagidani, and M. Ando (Editors), A. A. Balkema, Rotterdam, 173–184.

Ouillon, G., and D. Sornette (2005). Magnitude-dependent Omori law: Theory and empirical study, *J. Geophys. Res.* **110,** B04306, doi 10.1029/2004JB003311.

Plenkers, K., G. Kwiatek, M. Nakatani, G. Dresen, and JAGUARS-Group (2010). Observation of seismic events with frequencies $f > 25$ kHz at Mponeng deep gold mine, South Africa, *Seismol. Res. Lett.* **81,** no. 3, 467–479.

Sato, T., and T. Hirasawa (1973). Body wave spectra from propagating shear cracks, *J. Phys. Earth* **21,** 415–431.

Spottiswoode, S. M., and A. McGarr (1975). Source parameters of tremors in a deep-level gold mine, *Bull. Seismol. Soc. Am.* **65,** 93–112.

Takanami, T., and G. Kitagawa (1988). A new efficient procedure for the estimation of onset times of seismic-waves, *J. Phys. Earth* **36,** 267–290.

Yabe, Y., J. Philipp, M. Nakatani, G. Morema, M. Naoi, H. Kawakata, T. Igarashi, G. Dresen, H. Ogasawara, and JAGUARS-Group (2009). Observation of numerous aftershocks of an M_w 1.9 earthquake with an AE network installed in a deep gold mine in South Africa, *Earth Planets Space* **61,** e49–e52.

Yamada, T., J. J. Mori, S. Ide, H. Kawakata, Y. Iio, and H. Ogasawara (2005a). Radiation efficiency and apparent stress of small earthquakes in a South African gold mine, *J. Geophys. Res.* **110,** B01305, doi 10.1029/2004JB003221.

Yamada, T., J. J. Mori, S. Ide, H. Kawakata, Y. Iio, and H. Ogasawara (2005b). Correction to "Radiation efficiency and apparent stress of small earthquakes in a South African gold mine", *J. Geophys. Res.* **110,** B06301, doi 10.1029/2005JB003789.

Yamada, T., J. J. Mori, S. Ide, R. E. Abercrombie, H. Kawakata, M. Nakatani, Y. Iio, and H. Ogasawara (2007). Stress drops and radiated seismic energies of microearthquakes in a South African gold mine, *J. Geophys. Res.* **112,** B03305, doi 10.1029/2006JB004553.

Earthquake Research Institute
The University of Tokyo
1-1-1 Yayoi, Bunkyo
Tokyo 113-0032, Japan
(M.N., M.N., T.I.)

Research Center for Prediction of Earthquakes and Volcanic Eruptions
Graduate School of Science
Tohoku University
Aoba-ku, Sendai 980-8578, Japan
(Y.Y.)

Helmholtz Centre Potsdam
GFZ German Research Centre for Geosciences
Telegrafenberg
14473 Potsdam, Germany
(G.K., K.P.)

Manuscript received 18 December 2010